An Investigation of the Fe-Mn-Si System for Li-Ion Battery Negative Electrodes

An Investigation of the Fe-Mn-Si System for Li-Ion Battery Negative Electrodes

Yidan Cao,[1,2,z] Benjamin Scott,[2,*] R.A. Dunlap,[1,3,4] Jun Wang,[2] and M. N. Obrovac [1,2,3,,z]**

[1]*Department of Physics and Atmospheric Science, Dalhousie University, Halifax, Nova Scotia B3H 4R2, Canada*
[2]*Department of Chemistry, Dalhousie University, Halifax, Nova Scotia B3H 4R2, Canada*
[3]*Clean Technologies Research Institute, Dalhousie University, Halifax, Nova Scotia B3H 4R2, Canada*
[4]*College of Sustainability, Dalhousie University, Halifax, Nova Scotia B3H 4R2, Canada*

Fe-Mn-Si alloys prepared by ball milling were investigated as negative electrodes for Li-ion batteries. X-ray diffraction and room temperature ^{57}Fe Mössbauer measurements were used to characterize alloy structure, which revealed the formation of ternary $(Fe,Mn,)_{11}Si_{19}$ solid solutions. During cycling in Li cells, the formation of crystalline $Li_{15}Si_4$ was effectively suppressed by inactive transition metal silicide phases, resulting in good cycling performance. In addition, Fe was found to be superior to Mn in avoiding excessive side reactions with electrolyte during cycling.

 [DOI: 10.1149/2.1111816jes]

Manuscript submitted September 26, 2018; revised manuscript received December 4, 2018. Published January 3, 2019.

Si-based negative electrode materials are of interest for use in Li-ion rechargeable batteries due to their high volumetric capacity (2194 Ah/L) and low average voltage vs Li/Li^+.[1] Therefore, pure silicon electrodes have been studied in detail.[2–7] However, the cycling performance of pure silicon is poor when it is cycled to its full capacity due to its large volume expansion (280%) during lithiation and crystalline $Li_{15}Si_4$ formation at low potential.[3] Incorporating silicon with other elements is an effective route to improve the cycling performance of silicon by reducing volume expansion and suppressing $Li_{15}Si_4$ formation.[1,8–11] $Li_{15}Si_4$ phase suppression during the lithiation of Si alloyed with an inactive phase has been attributed to the large internal stresses within the active/inactive particle that exist when the active Si phase expands in contact with a fixed inactive phase.[12,13] Numerous Si-containing alloy negative electrode materials have been extensively studied as negative electrodes to improve the cycling performance of silicon, including: Si-Sn,[10] Si-Fe,[11,14] Si-Mn,[15,16] Si-Fe-Zn,[17,18] Si-Al-Mn[19]. When made by sputtering or ball milling, such alloys typically form active Si / inactive matrix nanostructured composites, where the inactive matrix comprises a transition metal silicide.[3,20] Most transition metal silicides have been found to be completely inactive or have very limited capacity at room temperature.[3,21–23] However, $NiSi_2$ has been found to be electrochemically active, when its grain size is small.[20]

Among the transition metals, iron and manganese are promising candidates for Si-TM alloys considering their low cost and high earth abundance. The binary systems, including Si-Fe and Si-Mn, have been previously studied in our group and by others.[11,13,15,16] Recently Du et al. have shown that sputtered Si-Fe alloy thin films comprise an active Si phase and an inactive Fe phase for Fe contents less than 23 atomic %. At higher Fe contents, $FeSi_2$ is formed as an inactive phase.[13] We have recently investigated the Si-Mn system and found that inactive $Si_{19}Mn_{11}$ is formed in high-Si content Si-Mn ball milled alloys.[16] The $Si_{75}Mn_{25}$ composition was demonstrated to have the highest volumetric capacity while maintaining good capacity retention.

To our knowledge ternary Fe-Mn-Si alloys have not been studied. Such alloys are interesting since, although iron and manganese have similar atomic radii, their silicides have completely different structures. Therefore, it is meaningful to discover what phases might be formed in this ternary system and if the ternary combination would induce higher disorder/amorphization during ball milling. Here, ball milled Fe-Mn-Si ternary alloys are studied in the composition range defined by the $Si_{85}Fe_{15}$ - $Si_{75}Mn_{25}$ tie line in the phase diagram. The phase and solid solution behavior in this composition range are reported and the electrochemistry of the resulting alloys are studied in lithium cells.

Experimental

$Fe_xMn_ySi_{100-x-y}$ $((x,y) = (15,0), (12,5), (9,10), (6,15), (3,20), (0,25))$ alloys were prepared by ball milling. These compositions are labeled in the Fe-Mn-Si phase diagram as shown in Figure 1. A total of 0.5 mL of silicon powder (Sigma-Aldrich, −325 mesh, 99%), iron powder (Alfa Aesar, −325 mesh, 98%) and manganese powder (Alfa Aesar, −325 mesh, 99.95%) were loaded into 65 ml hardened steel vials in stoichiometric ratios. The sample vials were sealed in an Ar atmosphere. Duplicate samples were ball milled simultaneously in a SPEX 8000D dual mixer mill for 4 hours under the optimal milling conditions as described in Reference 24, with the vial positions being switched at 2 hour intervals during milling. After milling, the powders were recovered from the vials by ethyl alcohol and dried in air at 120°C for 2 hrs.

X-ray diffraction patterns were collected at room temperature using a Rigaku Ultima IV diffractometer equipped with a diffracted beam graphite monochromator and using Cu K-alpha radiation. For ex-situ XRD patterns, $Fe_6Mn_{15}Si_{79}$ and $Fe_{12}Mn_5Si_{83}$ electrodes were lithiated to 5 mV and then delithiated to 0.9 V, and $Fe_{15}Si_{85}$ electrodes

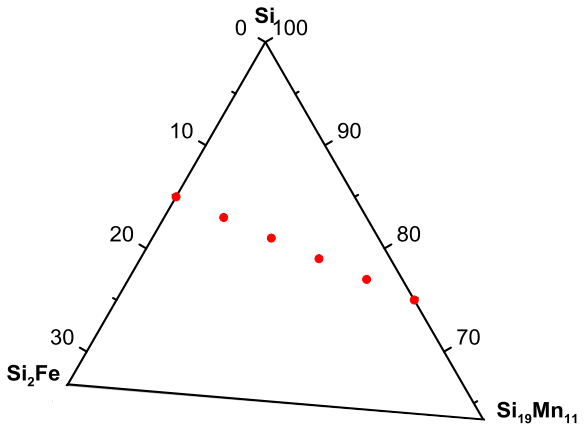

Figure 1. Composition of ball milled samples overlaid on a truncated Fe-Mn-Si ternary phase diagram.

*Electrochemical Society Student Member.
**Electrochemical Society Member.
[z]E-mail: yidancao@dal.ca; mnobrovac@dal.ca

were cycled 19 times between 5 mV and 0.9 V and then lithiated to 5 mV. The cycled cells were disassembled in an Ar-filled glovebox, and the electrodes were washed in DMC. Without exposure to air, cycled materials were scraped from the electrodes, placed onto a Si zero-background wafer, dried under vacuum and then sealed in a gas-tight XRD sample holder under Ar gas. Each XRD scan was collected from 10° to 90° 2-theta in 0.05° increments for 3 seconds per step. True sample densities were measured in He gas using a Micromeritics AccuPyc II 1340 gas pycnometer.

Room temperature ^{57}Fe Mössbauer effect measurements were performed using a SEE Co. constant acceleration spectrometer equipped with a Rh ^{57}Co source. For Mössbauer measurements, powder samples were transferred to a sample holder and heat sealed in aluminized mylar under Ar. Mössbauer data were collected at ±2 mm/s velocity scales calibrated relative to room temperature α-Fe. All Mössbauer spectra were analyzed with the Recoil software package (1998 Ken Lagarec and Denis G. Rancourt). Peaks were fit by Voigt-based fitting analysis with linearly correlated isomer shift and splitting parameters.[25]

Electrode slurries were prepared by mixing Fe-Mn-Si alloys, carbon black (Imerys Graphite and Carbon, Super C65) and a 10 weight % aqueous solution of lithium polyacrylate (LiPAA) (made by neutralizing a polyacrylic acid solution (Sigma-Aldrich, average molecular weight~250,000 g/mole, 35 wt% in H_2O) with LiOH $\cdot H_2O$ (Sigma Aldrich, 98%) in distilled water) with a volumetric ratio of 70/5/25 in distilled water. Slurries were mixed for one hour in a Retsch PM200 planetary mill at 100 rpm with three 13 mm tungsten carbide balls and then spread onto copper foil (Furukawa Electric, Japan) with a 0.004 inch gap coating bar. Then the coatings were dried in air for 1 hour at 120°C and cut into 1.3 cm disks and then heated under Ar for 1 hour at 120°C with no further air exposure.

Electrodes were assembled in 2325-type coin cells with a lithium foil counter/reference electrode. Two layers of Celgard 2300 separator were used in each coin cell. 1 M $LiPF_6$ (BASF) in a solution of ethylene carbonate, diethyl carbonate and monofluoroethylene carbonate (volume ratio 3:6:1, all from BASF) was used as electrolyte. Cell assembly was carried out in an Ar-filled glove box. Cells were cycled galvanostatically at 30.0 ± 0.1°C between 5 mV and 0.9 V using a Maccor Series 4000 Automated Test System at a C/20 rate and C/40 trickle discharge for the 1st cycle and a C/5 rate for the following cycles with a C/20 trickle discharge (lithiation).

Results and Discussion

Structural characterization.—The Fe-Mn-Si compositions made in this work are located along the $Si_{85}Fe_{15}$ - $Si_{75}Mn_{25}$ tie line, as indicated on the Fe-Mn-Si phase diagram[26] in Figure 1. According to the equilibrium phase diagram, these alloys should consist of Si, Si_2Fe and $Si_{19}Mn_{11}$. XRD profiles of the milled samples are shown in Figure 2. The peak positions of the β-Si_2Fe, α-Si_2Fe and $Si_{19}Mn_{11}$ alloy phases are labelled in the figure. In order to understand phase behavior in greater detail, the intensity of each phase in the samples were determined by fitting the XRD patterns. A representative fitting result from the $Fe_{12}Mn_5Si_{83}$ alloy is shown in Figure 3a. In the fits, a 5th order polynomial background function was used. Pseudo-Voigt peak shape functions were used to fit each peak. The relative integrated peak areas were fixed for each phase, according to their reference patterns in the ICSD database. Lattice constants of each phase were allowed to vary, which determined peak positions. Peak widths were fit according to the Caglioti formula. Figure 3b shows how the relative amount of each phase changes with Mn/Fe content. From the XRD results, it is clear that the ball milled alloys do not follow the predictions of the equilibrium phase diagram, which predicts Si- α-$FeSi_2$ 2-phase coexistence at room temperature. The most Si rich sample, $Fe_{15}Si_{85}$ has an XRD pattern that is primarily amorphous Si (a-Si), but also contains high (α-) and low temperature (β-) $FeSi_2$ phases, with the β-$FeSi_2$ phase dominating. The α-$FeSi_2$ phase is highly ordered with Fe and Si atoms each arranged in planes of square lattices in a Fe-Si-Si layer stacking sequence, each Fe coordinated to eight Si atoms in a cube with a slight tetragonal distortion. In contrast, the β-$FeSi_2$ phase has a more disordered structure, with many partially occupied lattice positions. In β-$FeSi_2$ the Fe atoms are also 8-coordinated, but by Si in a highly distorted cube. In the $Si_{85}Fe_{15}$ sample, the formation of β-$FeSi_2$ is favored over α-$FeSi_2$. This is perhaps due to a high level of defects introduced by the ball milling process, which favors the disordered structure. Unexpectedly, increasing the Mn content to 5 at. % results in a preference for the formation of the α-$FeSi_2$ phase, but no Mn-Si phases are present. This suggests that some Mn may be substituting into $FeSi_2$ resulting the preferential formation of α-$FeSi_2$ during ball milling over the β-$FeSi_2$ phase. It is unknown why the presence of Mn creates a preference for the more ordered α-phase. At 10 at.% Mn, β-$FeSi_2$ phase formation is completely suppressed and the XRD pattern is composed chiefly of Si and α-$FeSi_2$, $Mn_{11}Si_{19}$ phases. For the samples with more than 10 at.% Mn, only a-Si and $Mn_{11}Si_{19}$ diffraction peaks can be observed. This can be more clearly seen in Figure 2b. At this composition the α-$FeSi_2$ phase must be saturated with Mn. This corresponds to a fully saturated α-$FeSi_2$ phase composition of approximately α-$(Fe_{0.58}Mn_{0.42})Si_2$.

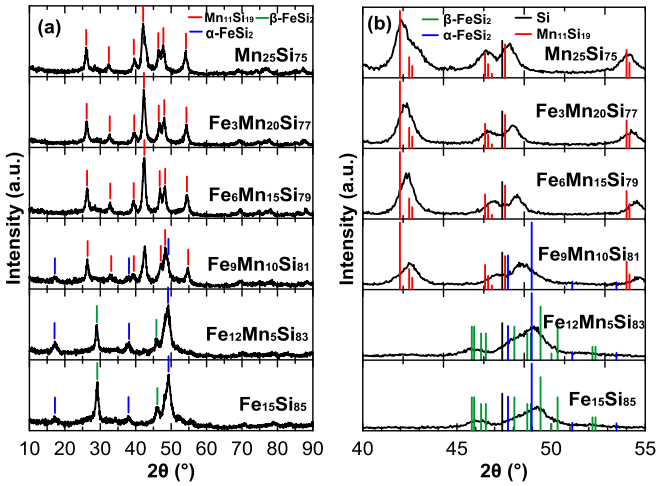

Figure 2. XRD patterns of Fe-Mn-Si alloys measured in the range of (a) 10–90°, and (b) 40–55°.

As the Mn content is increased further and the Fe content is decreased, the $Mn_{11}Si_{19}$ peaks shift to lower angles. This is shown more clearly in Figure 2b, which shows enlarged diffraction patterns in the region from 40° to 55°. At 15 at. % Mn the $Mn_{11}Si_{19}$ peaks shift to lower angles and peaks from $FeSi_2$ phases are completely absent. Increasing the Mn content and decreasing the Fe content further results in a further shift to lower angles, until the XRD pattern corresponds to the lattice constant of $Mn_{11}Si_{19}$ for the sample containing no Fe. Figure 3c shows the lattice constants of the $Mn_{11}Si_{19}$ phase as a function of composition in samples with ≥ 10 at. % Mn. As the Fe content is increased, the a and c lattice constants decrease linearly, consistent with $(Fe, Mn)_{11}Si_{19}$ solid solution formation. This is also consistent with the absence of any Fe-Si phases in this composition region. The $Mn_{11}Si_{19}$ structure is similar to the α and β-$FeSi_2$ structures, in that Mn is also coordinated by 8 Si, but in a highly distorted cubic geometry. This may explain why Fe atoms can be accommodated in this structure. The decrease in lattice constants with increasing Mn content, may be due to the smaller size of Mn (1.12 Å) compared to Fe (1.23 Å), according to Vegard's law.

The observed phase behavior of the ball milled samples is summarized in Figure 3d in terms of the parameter x in $Fe_{1-x}Mn_x$, with an error in x of about ± 0.1, due to the coarseness in sampling. The diagram illustrates the non-equilibrium state of the system after ball milling. In the high Fe region of the diagram, the three phases Si, β-$FeSi_2$, and α-$(Fe_{1-x}Mn_x)Si_2$ ($0 \le x \le 0.42$) coexist. At high Mn contents Si is in coexistence with the $(Mn_xFe_{1-x})_{11}Si_{19}$ ($0.63 \le x \le 1.0$) solid solution. Between these compositions Si is in coexistence with

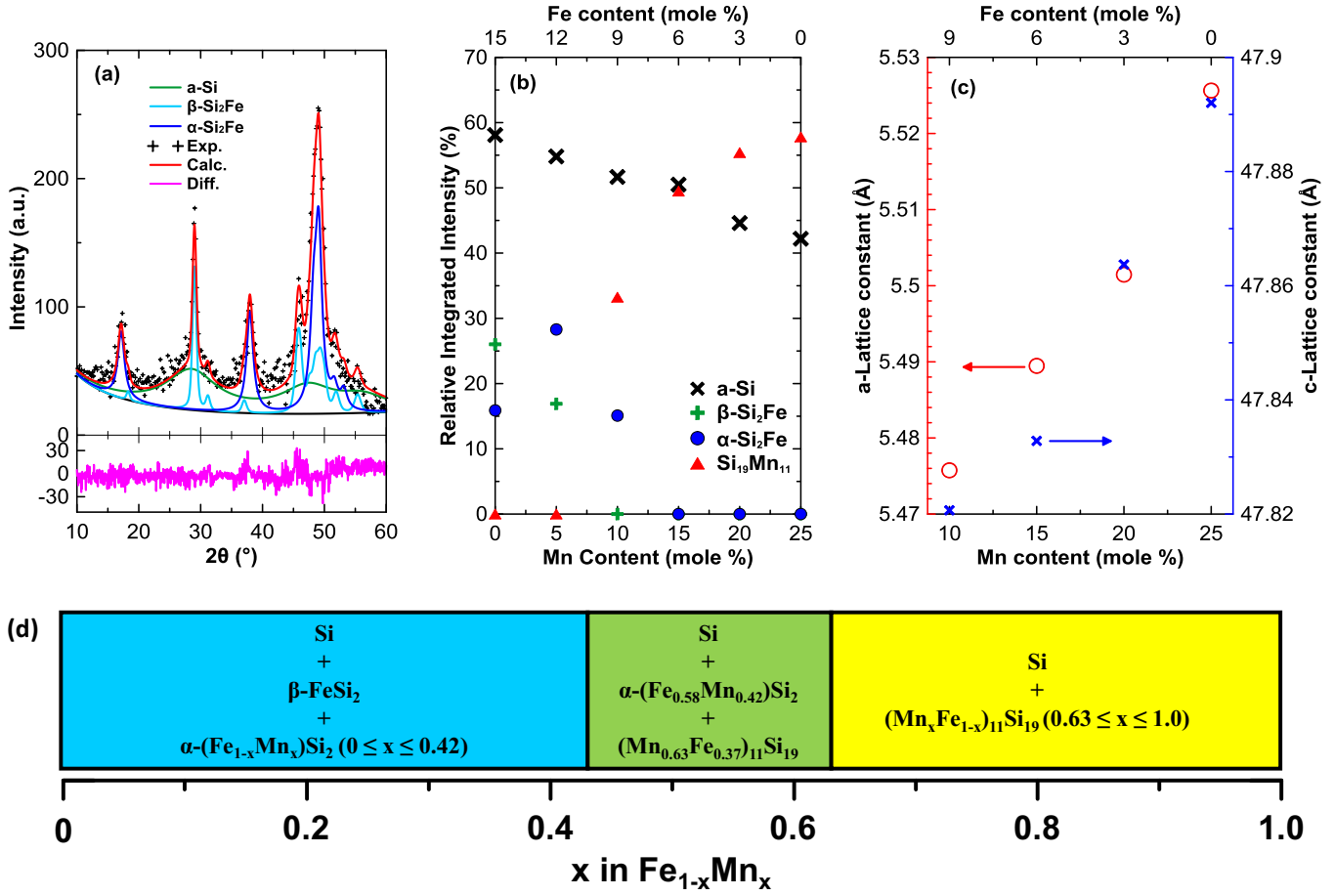

Figure 3. (a) The XRD profile of $Fe_{12}Mn_5Si_{83}$ fitted as described in the text. (b) Relative integrated intensity of different phases in Fe-Mn-Si alloy samples. (c) Lattice constants of the $Mn_{11}Si_{19}$ phase in Fe-Mn-Si alloys as a function of composition along the $Si_{85}Fe_{15}$ - $Si_{75}Mn_{25}$ tie line. (d) The observed phase behavior during ball milling compositions along the $Si_{85}Fe_{15}$ - $Si_{75}Mn_{25}$ tie line.

saturated solid solutions having compositions approximately equal to α-$(Fe_{0.58}Mn_{0.42})Si_2$ and $(Mn_{0.63}Fe_{0.37})_{11}Si_{19}$. To our knowledge this is the first report of Mn solubility in α-$FeSi_2$ and Fe solubility in $Mn_{11}Si_{19}$.

To more carefully characterize the microstructure of the ball milled samples, ^{57}Fe Mössbauer experiments were performed. Mössbauer spectra of all samples are shown in Figure 4a. All Mössbauer spectra were fit to one quadrupole site distribution. The quadrupole doublet shifts to lower velocity with increasing Fe content, which indicates an increase in electron density at the Fe nucleus.[27] This trend is plotted in Figure 4b and will be discussed below. The isomer shift (δ) decreases from +0.276 mm/s to +0.125 mm/s with increasing Fe content. The dependence of the mean quadrupole splitting (Δ) on the Fe content is also shown in Figure 4b. The value of Δ increases from 0.435 mm/s to 0.507 mm/s with increasing Fe content. As discussed above, Fe related phases are not detected by XRD in $Fe_6Mn_{15}Si_{79}$ and $Fe_3Mn_{20}Si_{77}$. Here, Mössbauer spectra suggest that all of the Fe atoms exist in compounds rather than in the elemental state and the linear trend in Mössbauer fitting parameters shown in Figure 4b suggests solid solution formation.

According to previous studies, the isomer shift of β-$FeSi_2$ is less than +0.100 mm/s.[28,29] Reported isomer shift values of α-$FeSi_2$ are around +0.260 mm/s, based on measurements of either crystalline α-$FeSi_2$ or thin films.[28,30] These values may not be the same for ball milled alloys. In order to determine the isomer shift of balled milled α-$FeSi_2$, crystalline α-$FeSi_2$ was synthesized by arc-melting a stoichiometric ratio of Fe and Si and the resulting ingot was ground by mortar and pestle into a powder. The resulting material had an XRD pattern consistent with α-$FeSi_2$ with a small FeSi impurity ('arc-melting' in Figure S1). Its Mössbauer spectrum is shown in Figure S2. By this means, the isomer shift of crystalline α-$FeSi_2$ was determined to be +0.239 mm/s. The crystalline α-$FeSi_2$ was then ball milled for 4 hours ('arc-melting + ball milling' in Figure S1), resulting in the formation of nanocrystalline α-$FeSi_2$ and FeSi, according to its XRD pattern. The isomer shift of the resulting powder was measured to be +0.201 mm/s, which is lower than the isomer shift of crystalline α-$FeSi_2$. This value is comparable with that found for mechanically milled $Fe_{0.8}Si_2$ reported by Dézsi et al.[30] It should be noted that the increased content of FeSi in this sample is expected to increase the isomer shift, since it has been observed that lowering the Fe content in Fe-Si alloys results in an increased isomer shift.[25] Therefore, the decreased isomer shift observed here must be due to changes in the α-$FeSi_2$ phase and demonstrates that the electron density is higher in ball milled α-$FeSi_2$, than its crystalline state. In contrast, ball milling a 2:1 molar ratio of Si and Fe powders results in the exclusive formation of the β-$FeSi_2$ phase according XRD ('ball milling' shown in Figure S1). The isomer shift of this sample was determined to be +0.139 mm/s which is consistent with the lower isomer shift observed for β-$FeSi_2$ compared to α-$FeSi_2$, as reported previously.[28,29]

According to the XRD results shown in Figure 3b, the $Fe_{15}Si_{85}$ alloy consists of a-Si and β-$FeSi_2$ and α-$FeSi_2$ phases, with the β-$FeSi_2$ phase dominating. As the Mn content is increased and the Fe content is decreased, the relative amount of the β-$FeSi_2$ phase decreases and the α-$FeSi_2$ phase begins to dominate. This would tend to result in an increase in the isomer shift on account of the higher isomer shift of the α-$FeSi_2$ phase, which is indeed the case. For samples with Mn contents greater than 10 at %, only XRD diffraction peaks of a-Si and $Mn_{11}Si_{19}$ are observed. Both the linear trend in the XRD lattice constants and the

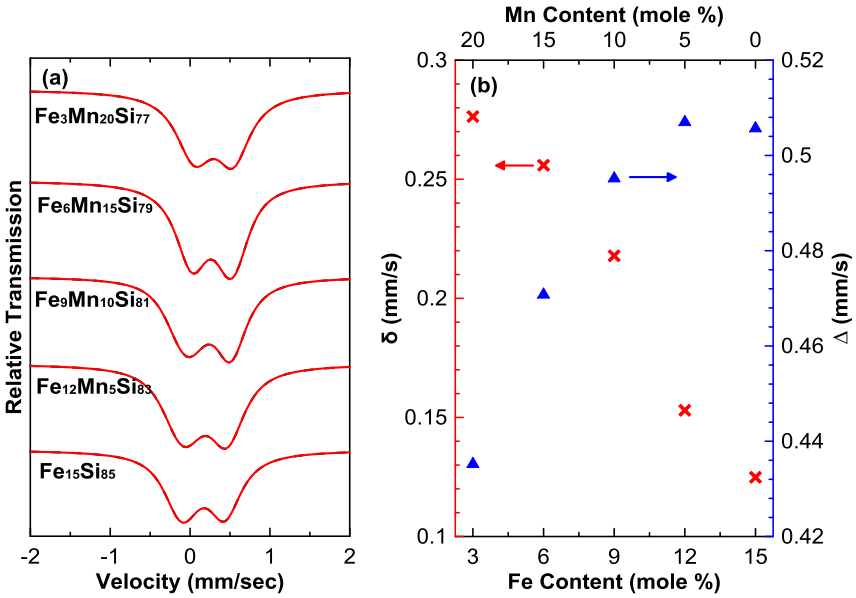

Figure 4. (a) Mössbauer spectra of Fe-Mn-Si alloys. The data are shown in black and fits are shown in red. (b) Isomer shift (δ) relative to room temperature α-Fe and mean quadrupole splitting (Δ) for all spectra that were fit to a distribution of doublets as a function of composition.

^{57}Fe Mössbauer peak parameters suggest solid solution formation with Fe substitution in $Mn_{11}Si_{19}$ phase. The higher values of isomer shifts with increasing Mn content indicate a further decrease of electron density. As the more electron rich Fe is replaced by Mn, the electron density of Fe atoms would be decreased with increasing concentration of Mn atoms in near neighbor sites. Vacancies in the samples would dilute the electron density around Fe and also lead to an increase in the isomer shift. Therefore, the increase in isomer shift with Mn content may indicate an increasing vacancy number in the samples with increasing Mn content. Variations in quadrupole splittings may also be associated with changes in the symmetry around the Fe nuclei with increasing Mn or vacancy contents.

Electrochemical performance.—Figure 5 shows voltage curves of Fe-Mn-Si alloy electrodes. Corresponding differential capacity curves are shown in Figure 6a. Only features corresponding to silicon are observed. This is consistent with these alloys being composed of an active Si phase and inactive silicide phases, which is typical of most Si-transition metal alloys.[1] In this case the inactive silicides are the β-$FeSi_2$, α-$FeSi_2$ and $Mn_{11}Si_{19}$ phases observed by XRD. This is also consistent with the alloys' observed capacity, as is shown below. This is further confirmed in Figure S3, which shows XRD patterns of alloys Fe-Mn-Si alloy electrodes prior to and after one discharge/charge cycle. The XRD patterns of the silicide phases in the cycled electrodes are the same as those before cycling, confirming that the Fe and Mn silicides are inactive. The irreversible capacities of all the alloys are about the same. Peaks at about 0.3 V are present in the differential capacity curves for all the samples during the first lithiation and are commonly ascribed to the nucleation and growth of Li-Si phases during initial lithiation.[1] These nucleation and growth peaks are sharp and distinct in $Fe_{15}Si_{85}$ and they become less pronounced with increasing Mn content. Increasing defects induced by the formation of ternary solid solutions may result in a more facile initial lithiation. However, the average lithiation and delithiation voltage of all samples were similar. Lithiation peaks at ~0.1 V and 0.21–0.25 V are related to lithiation plateaus of amorphous silicon, and broad delithiation peaks at ~0.3 V and ~0.5 V are from delithiation of amorphous silicon. Features only related to amorphous silicon are observed in the differential capacity of all the samples during the initial cycles. However, as cycling progresses, peaks appear near 0.45 V during delithiation, which are related to the delithiation of $Li_{15}Si_4$. At the same time, the delithiation peaks of $Li_{15}Si_4$ phase are divided into two peaks centered at around 0.38 V and 0.42 V. These two peaks are less pronounced in samples with higher Mn content.

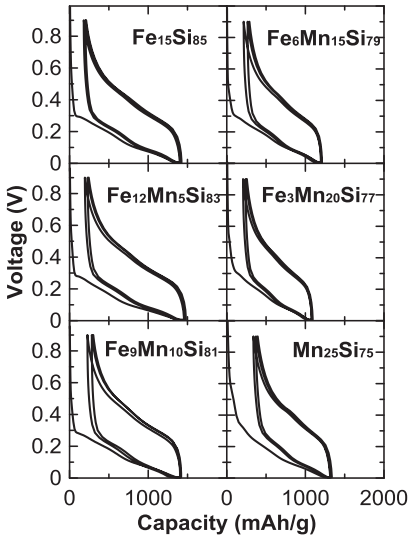

Figure 5. Voltage curves of Fe-Mn-Si alloys.

In order to better understand the formation of $Li_{15}Si_4$ during cycling, the relative content of $Li_{15}Si_4$ phase and percent of each $Li_{15}Si_4$ peak were calculated by noting that $Li_{15}Si_4$ delithiation occurs only in the 0.36–0.48 V range. The fraction of $Li_{15}Si_4$ phase formed during cycling is therefore related to delithiation capacity in the 0.36–0.48 V range by the total delithiation capacity. When no $Li_{15}Si_4$ phase is formed, this ratio is equal to about 0.2. When only $Li_{15}Si_4$ phase is formed, this ratio is equal 1. Therefore, the amount of $Li_{15}Si_4$ phase is formed can be approximated by:

$$f = (Q_{0.36-0.48\ V}/Q_{tot} - 0.2)/0.8 \times 100\% \quad [1]$$

Where f is the percent of the active Si present that has formed $Li_{15}Si_4$ at full lithiation. The results are shown in Figure 6b. In all compositions, the $Li_{15}Si_4$ is formed after only a few cycles and its content increases as cycling progresses, then reaches a plateau. For $Fe_{15}Si_{85}$, the plateau is reached after ~25 cycles and it has the highest $Li_{15}Si_4$ content (~46 at. % of the active Si present). With higher Mn content, the plateaus are reached after ~30 cycles and the percent $Li_{15}Si_4$ formed is reduced to little as 25 at. % of the active Si, suggesting better suppression of $Li_{15}Si_4$ formation.

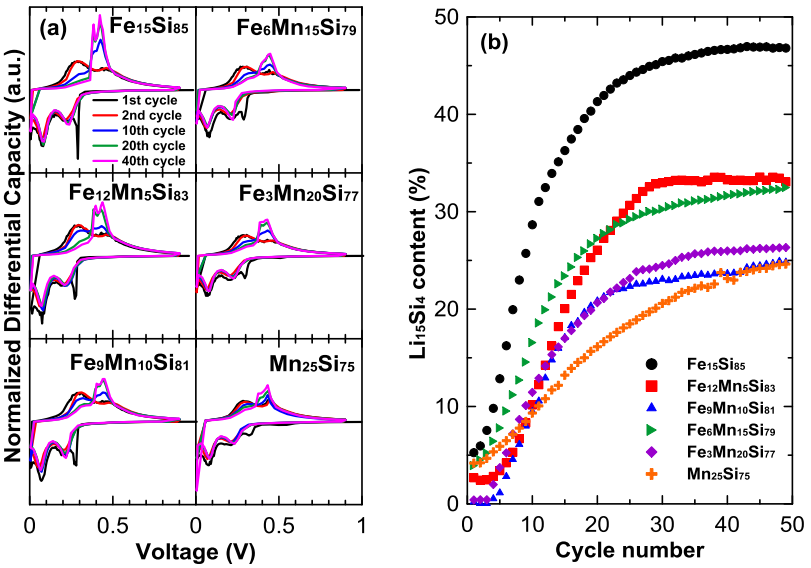

Figure 6. (a) Differential capacity curves of Fe-Mn-Si alloys. (b) The percent of the active Si present that has formed $Li_{15}Si_4$ after full lithiation (as determined by Equation 1) vs. cycle number.

The splitting of the $Li_{15}Si_4$ delithiation peak observed in Figure 6a is unexpected. To our knowledge, this is the first observation of the splitting of the $Li_{15}Si_4$ delithiation peak. We have observed these two peaks for this system and other Si-M systems that we plan to report shortly. The amount of peak splitting changes, depending on the metal M. It also becomes more severe as the alloy grain size is decreased. In order to investigate if the $Li_{15}Si_4$ phase is somehow different for the phases showing $Li_{15}Si_4$ delithiation peak splitting, the cell with the most obvious peak splitting, $Fe_{15}Si_{85}$, was disassembled after its 20th lithiation. The electrode powder was collected and sealed in an Ar atmosphere. Its differential capacity curve is shown in Figure S4(a) and its XRD pattern is shown in Figure S4(b). For comparison, the differential capacity curve and XRD pattern of a fully lithiated pure silicon electrode for which $Li_{15}Si_4$ delithiation peak splitting is not observed is also shown. Both XRD patterns show diffraction peaks attributed to $Li_{15}Si_4$ phase. The only difference between the two being the presence of the inactive $FeSi_2$ phases in the $Fe_{15}Si_{85}$ pattern. In summary, the peak splitting is not due to the formation of any phases other than $Li_{15}Si_4$, it is correlated with the presence of the inactive silicide phase, changing the chemistry of the inactive silicide phase, changes the amount of splitting and the amount of splitting increases with decreasing alloy grain size. We suggest that the peak splitting arises from the different environments in $Li_{15}Si_4$ at the $Li_{15}Si_4$/metal silicide contact region compared to in the bulk of the small $Li_{15}Si_4$ grains. This explanation is consistent will all the above observations related to the peak splitting, since changing the grain size and the inactive phase should both affect the $Li_{15}Si_4$/metal silicide interface region and the degree of splitting, as observed. However, further work is needed to verify this model directly.

Figure 7 shows the reversible (first delithiation) capacity of the Fe-Mn-Si alloys plotted as a function of Si content. As the Si content is increased, the capacity increases accordingly. Also shown is the theoretical capacity based on the formation of active Si, inactive $Mn_{11}Si_{19}$, and inactive $FeSi_2$, as indicated by XRD and Mössbauer results, where the active Si phase was assumed to alloy with 3.75 Li.[3] The predicted and experimental capacities follow the same general trend confirming the model, however the observed reversible capacities are less than the predicted capacities for high capacity samples. These capacities correspond to volumetric capacities from 1600–1900 Ah/L and volume expansions from about 130–175%. The lower values of the reversible capacities for high capacity samples is likely due to their higher volume expansion, which can cause mechanical failure of the alloy or the composite electrode during cycling.

Cycling performance of all alloys in this work is shown in Figure 8a, and their coulombic efficiencies are shown in Figure 8b. The cycling performance of all the alloys is good in the 50 cycles tested. The coulombic efficiency (CE) for the $Fe_{15}Si_{85}$ alloy is highest, at about 99.5%. The CE becomes lower as the Mn content is increased, indicating a higher level of parasitic electrolyte decomposition reactions. We have found previously that different inactive phases can catalyze electrolyte decomposition at the negative electrode.[31] The results here imply that the rate of electrolyte decomposition on the alloy surface is low when Fe is present in the alloy, but is enhanced when Mn is present in the alloy. On this basis, the use of Mn in Si-alloy negative electrodes should be avoided.

Conclusions

Ball milled Fe-Mn-Si ternary alloys were studied in the composition range defined by the $Fe_{15}Si_{85}$ - $Mn_{25}Si_{75}$ tie line and tested as negative electrodes in Li half cells. The most Si rich composition ($Fe_{15}Si_{85}$) was found to comprise amorphous Si with β-$FeSi_2$ and α-$FeSi_2$. As the Mn content was increased the amount of α-$FeSi_2$ increased and then features of a ternary solid solution having the $Mn_{11}Si_{19}$ structure was observed. To our knowledge, this is the first

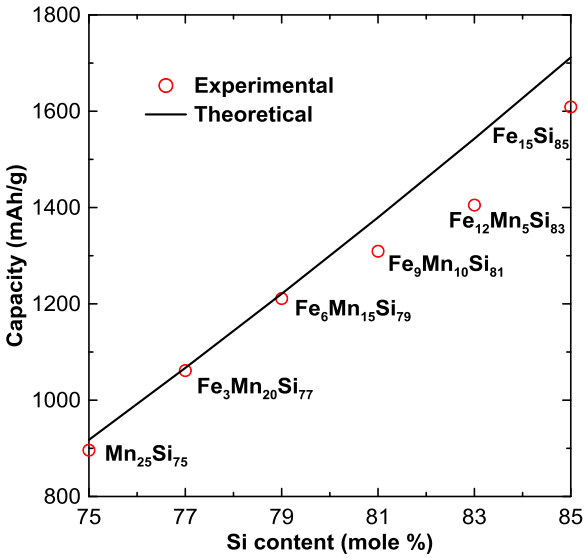

Figure 7. The reversible capacity of Fe-Mn-Si alloys as a function of Si content. Also shown is a line representing the theoretical alloy capacity, as described in the text.

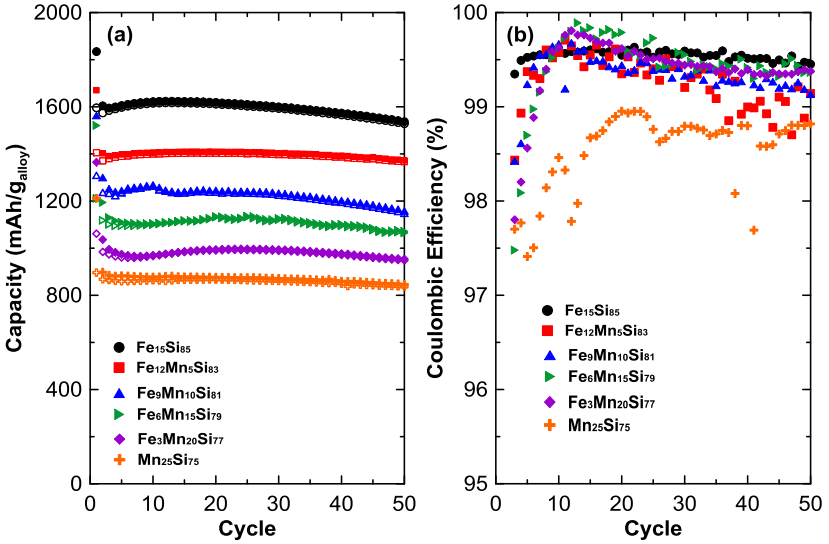

Figure 8. (a) Cycling performance and (b) coulombic efficiency of Fe-Mn-Si alloys.

observation of a $(Fe, Mn)_{11}Si_{19}$ solid solution. This phase model was consistent with the observed capacities of the alloys in Li cells. While all alloys showed good cycling performance, the coulombic efficiency of the alloys was highest for the $Fe_{15}Si_{85}$ alloy and became lower with increasing Mn content; the $Mn_{25}Si_{75}$ alloy having the lowest coulombic efficiency despite having the lowest capacity and lowest volume expansion. This indicates that the presence of Mn accelerates electrolyte decomposition on the alloy surface and should be avoided.

Acknowledgments

The authors would like to acknowledge funding from NSERC and 3M Canada, Co. under the auspices of the Industrial Research Chair program. We also acknowledge the support of the Canada Foundation for Innovation, the Atlantic Innovation Fund and other partners that fund the Facilities for Materials Characterization managed by the Institute for Research in Materials, and Dr. Jeff Dahn for use of the pycnometer. Yidan Cao acknowledges financial support from the Killam Trusts.

ORCID

M. N. Obrovac https://orcid.org/0000-0001-5509-3185

References

1. M. N. Obrovac and V. L. Chevrier, *Chem. Rev.*, **114**, 11444 (2014).
2. T. D. Hatchard and J. R. Dahn, *J. Electrochem. Soc.*, **151**, A838 (2004).
3. M. N. Obrovac and L. Christensen, *Electrochem. Solid-State Lett.*, **7**, A93 (2004).
4. J. Li and J. R. Dahn, *J. Electrochem. Soc.*, **154**, A156 (2007).
5. U. Kasavajjula, C. Wang, and A. J. Appleby, *J. Power Sources*, **163**, 1003 (2007).
6. M. N. Obrovac and L. J. Krause, *J. Electrochem. Soc.*, **154**, A103 (2007).
7. K. L. Lee, J. Y. Jung, S. W. Lee, H. S. Moon, and J. W. Park, *J. Power Sources*, **129**, 270 (2004).
8. T. D. Hatchard, M. N. Obrovac, and J. R. Dahn, *J. Electrochem. Soc.*, **152**, A2335 (2005).
9. T. D. Hatchard and J. R. Dahn, *J. Electrochem. Soc.*, **152**, A1445 (2005).
10. T. D. Hatchard and J. R. Dahn, *J. Electrochem. Soc.*, **151**, A1628 (2004).
11. M. D. Fleischauer, J. M. Topple, and J. R. Dahn, *Electrochem. Solid-State Lett.*, **8**, A137 (2005).
12. D. S. M. Iaboni and M. N. Obrovac, *J. Electrochem. Soc.*, **163**, A255 (2016).
13. Z. Du, R. A. Dunlap, and M. N. Obrovac, *J. Electrochem. Soc.*, **163**, A2011 (2016).
14. H. Dong, R. X. Feng, X. P. Ai, Y. L. Cao, and H. X. Yang, *Electrochim. Acta*, **49**, 5217 (2004).
15. P. Zuo and G. Yin, *J. Alloys Compd.*, **414**, 265 (2006).
16. Y. Cao, R. A. Dunlap, and M. N. Obrovac, *J. Electrochem. Soc.*, **165**, A1734 (2018).
17. L. MacEachern, R. A. Dunlap, and M. N. Obrovac, *J. Electrochem. Soc.*, **162**, A2319 (2015).
18. L. MacEachern, R. A. Dunlap, and M. N. Obrovac, *J. Electrochem. Soc.*, **162**, A229 (2014).
19. M. D. Fleischauer and J. R. Dahn, *J. Electrochem. Soc.*, **151**, A1216 (2004).
20. Z. Du, T. D. Hatchard, R. A. Dunlap, and M. N. Obrovac, *J. Electrochem. Soc.*, **162**, A1858 (2015).
21. H. Usui, K. Meabara, K. Nakai, and H. Sakaguchi, *Int. J. Electrochem. Sci.*, **6**, 2246 (2011).
22. H.-Y. Lee and S.-M. Lee, *J. Power Sources*, **112**, 649 (2002).
23. Y. S. Lee, J. H. Lee, Y. W. Kim, Y. K. Sun, and S. M. Lee, *Electrochim. Acta*, **52**, 1523 (2006).
24. T. D. Hatchard, A. Genkin, and M. N. Obrovac, *AIP Adv.*, **7** (2017).
25. J. D. McGraw, M. D. Fleischauer, J. R. Dahn, and R. A. Dunlap, *Philos. Mag.*, **86**, 5017 (2006).
26. *http://steel.kisti.re.kr/htm/Fe-Mn-Si.htm*.
27. L. R. Walker, G. K. Wertheim, and V. Jaccarino, *Phys. Rev. Lett.*, **6**, 98 (1961).
28. J. Desimoni and F. H. Sánchez, *Hyperfine Interact.*, **122**, 277 (1999).
29. G. K. Wertheim, J. H. Wernick, and D. N. E. Buchanan, *J. Appl. Phys.*, **37**, 3333 (1966).
30. I. Dézsi, C. Fetzer, L. Bujdosó, J. Brötz, and A. G. Balogh, *J. Alloys Compd.*, **508**, 51 (2010).
31. Z. Yan and M. N. Obrovac, **164**, 2977 (2017).